Broadband Minimum Variance Beamforming for Ultrasound Imaging

Holfort, Iben Kraglund; Gran, Fredrik; Jensen, Jørgen Arendt

Published in:
IEEE Transactions on Ultrasonics Ferroelectrics and Frequency Control

Link to article, DOI:
10.1109/TUFFC.2009.1040

Publication date:
2009

Document Version
Publisher's PDF, also known as Version of record

Broadband Minimum Variance Beamforming for Ultrasound Imaging

Iben Kraglund Holfort, *Student Member, IEEE*, Fredrik Gran, and Jørgen Arendt Jensen, *Senior Member, IEEE*

***Abstract*—A minimum variance (MV) approach for near-field beamforming of broadband data is proposed. The approach is implemented in the frequency domain, and it provides a set of adapted, complex apodization weights for each frequency subband. The performance of the proposed MV beamformer is tested on simulated data obtained using Field II. The method is validated using synthetic aperture data and data obtained from a plane wave emission. Data for 13 point targets and a circular cyst with a radius of 5 mm are simulated. The performance of the MV beamformer is compared with delay-and-sum (DS) using boxcar weights and Hanning weights and is quantified by the full width at half maximum (FWHM) and the peak-side-lobe level (PSL). Single emission {DS boxcar, DS Hanning, MV} provide a PSL of {−16, −36, −49} dB and a FWHM of {0.79, 1.33, 0.08} mm. Using all 128 emissions, {DS boxcar, DS Hanning, MV} provides a PSL of {−32, −49, −65} dB, and a FWHM of {0.63, 0.97, 0.08} mm. The contrast of the beamformed single emission responses of the circular cyst was calculated as {−18, −37, −40} dB. The simulations have shown that the frequency subband MV beamformer provides a significant increase in lateral resolution compared with DS, even when using considerably fewer emissions. An increase in resolution is seen when using only one single emission. Furthermore, the effect of steering vector errors is investigated. The steering vector errors are investigated by applying an error of the sound speed estimate to the ultrasound data. As the error increases, it is seen that the MV beamformer is not as robust compared with the DS beamformer with boxcar and Hanning weights. Nevertheless, it is noted that the DS does not outperform the MV beamformer. For errors of 2% and 4% of the correct value, the FWHM are {0.81, 1.25, 0.34} mm and {0.89, 1.44, 0.46} mm, respectively.**

I. Introduction

In medical ultrasound imaging, beamforming is conventionally carried out using the delay-and-sum (DS) beamformer. The aim of the DS beamformer is to maximize its output by delaying, weighting, and summing the individual sensor signals. The DS beamformer uses predefined, fixed apodization weights, which are independent of the input data. As is commonly known, an inherent compromise between the main-lobe width and the side-lobe level exists. Choosing a smoothing apodization function, such as Hanning, the side-lobe level can be reduced at the expense of a lateral broadening of the main-lobe.

For decades, data-dependent, adaptive beamformers have been used in other fields of array signal processing, e.g., sonar and radar. Whereas the conventional beamformer is a passive process using predefined, fixed, data-independent apodization weights, the adaptive beamformer actively updates a set of new apodization weights for each point in the image. These apodization weights are dependent on the input data. One of the widely used methods was originally introduced by Capon in 1969 [1]. The Capon or minimum variance (MV) beamformer continuously updates the apodization weights, so that the variance (or power) of the weighted sensor signals is minimized under the constraint that the signal emerging from the point of interest is passed without distortion.

Recently, the application of adaptive beamforming to the field of medical ultrasound imaging has become an area of increased interest. The adaptive beamformers potentially provide improvements of the image quality, in terms of lateral resolution and contrast. In 2002, Mann and Walker [2] introduced the linearly constrained adaptive beamformer, also referred to as the Frost beamformer [3]. They applied the method to experimental data of a single point target and a cyst phantom using diagonal loading to ensure a well-conditioned covariance matrix. Another approach to obtain a well-conditioned covariance matrix is to use spatial averaging, which was introduced to ultrasound data by Sasso and Cohen-Bacrie in 2005 [4]. They apply the minimum variance beamformer on a simulated cyst. Four different adaptive beamformers were introduced by Viola and Walker [5], and these were applied to simulated data. Synnevåg *et al.* [6] applied the MV beamformer to simulated and experimental ultrasound data, and they proposed a robust approach using diagonal loading. Wang *et al.* [7] also applied the MV beamformer as well as the MUltiple SIgnal Classification (MUSIC) approach. They introduce yet another approach to obtain a well-conditioned covariance matrix by averaging over several emissions from different spatial positions.

The previous work within this field is characterized by the fact that narrowband methods have been applied directly on broadband ultrasound data. Instead, this paper proposes an approach for near-field, adaptive beamforming of broadband data. Preliminary results of this method were presented in [8]. This approach is implemented in the frequency domain, and it provides a set of adapted, complex apodization weights for each frequency subband. Whereas the conventional method and the previous imple-

Manuscript received May 26, 2008; accepted September 6, 2008. This work was supported by grant 26-04-0024 from the Danish Science Foundation; grant 274-05-0327 from the Danish Research Agency, the Radiopartsfoundation, the Technical University of Denmark; and by B-K Medical ApS, Denmark.

I. K. Holfort and J. A. Jensen are with the Center for Fast Ultrasound Imaging, Department of Electrical Engineering, Technical University of Denmark, Lyngby, Denmark (e-mail: ikh@elektro.dtu.dk).

F. Gran is with GN ReSound A/S, Ballerup, Denmark.

Digital Object Identifier 10.1109/TUFFC.2009.1040

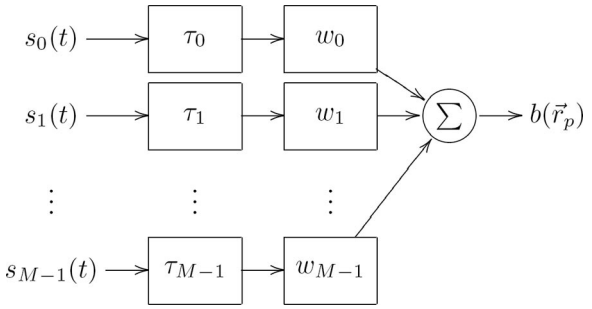

Fig. 1. Block diagram of the conventional delay-and-sum beamformer. The sensor signals are delayed, weighted, and subsequently summed to form the beamformer output.

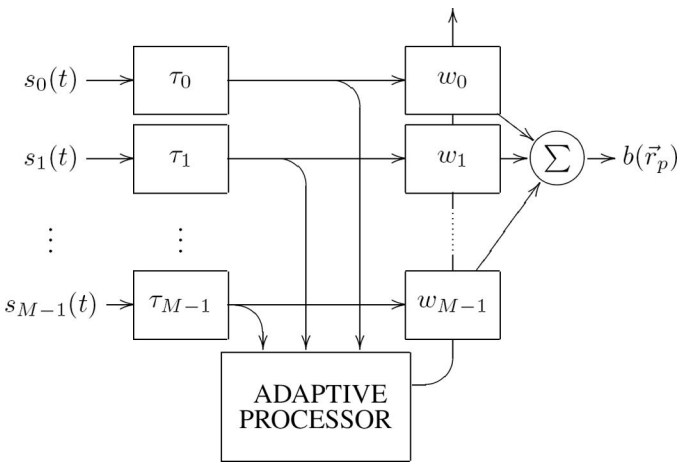

Fig. 2. Block diagram of an adaptive narrowband beamformer. The adaptive processor determines a set of optimized apodization weights from the delayed sensor signals.

mentations of the MV beamformer provide a single weight value for each sensor, this proposed method continuously updates a set of spatial filters for each sensor signal.

The outline of the paper is as follows: The method is presented in Section II. It is validated on simulated synthetic aperture ultrasound data and plane wave emission data. The results are given in Section III. In Section IV, the degradation of the point spread function dependent on incorrect sound speed estimates is investigated. Concluding remarks are given in Section V.

II. Method

Conventionally, beamforming is carried out on each of the sensor signals independently. As shown in Fig. 1, each sensor signal is delayed and weighted; and they are consecutively summed to form the beamformer output. The DS beamformer is a passive process using predefined, fixed, data-independent apodization weights. Because the phase-shift can be implemented as a time-delay, the DS beamformer works for both narrowband and broadband signals.

For narrowband signals, an adaptive beamformer is simply an extension to the DS beamformer, where the only difference is the choice of weights. Instead of using predefined weights, the adaptive processor actively updates a set of new apodization weights that are dependent on the delayed sensor signals. As illustrated in Fig. 2, the delayed sensor signals are fed to the adaptive processor, which determines a set of optimized weights for the specific, delayed sensor signals.

The adaptive process differs for the different adaptive beamformers. This paper concentrates on the minimum variance (MV) beamformer, which is described in Section II-C. For broadband signals, the signals are divided into a set of narrowband signals using the discrete Fourier transform; this approach is described in Section II-B.

A. Presteering

As in conventional beamforming, the sensor signals are presteered at the focus point, so that the sensor responses from the focus point will sum in phase, and the DS beamformer output from the current point will be maximized. Presteering at point $\vec{r}_p = (x_p, z_p)$ is carried out by compensating for the propagation delay profile for this point. The delay is calculated as the propagation path from the transmit element to the focus point and back to the mth receiving element. For a transducer array of M elements, the delay is given by

$$\tau_m(\vec{r}_p) = \frac{\| \vec{r}^{\,(\mathrm{xmt})} - \vec{r}_p \| + \| \vec{r}_m^{\,(\mathrm{rcv})} - \vec{r}_p \|}{c}, \qquad (1)$$

for $m = 0, 1, \ldots, M-1$, where c is the speed of sound, and $\vec{r}^{\,(\mathrm{xmt})}$ and $\vec{r}^{\,(\mathrm{rcv})}$ are the spatial positions of the transmitting and receiving elements, respectively. By compensating for the delay, the mth presteered sensor signal is given by

$$y_m(t) = s_m(t + \tau_m(\vec{r}_p)), \qquad (2)$$

where $s_m(t)$ is the received waveform on the mth sensor. By definition, the presteered signals, $y_m(t)$, are dependent on the focus point, $\vec{r}_p$. However, to simplify the notation, this dependence is omitted.

The concept of presteering is illustrated in Figs. 3(a)-(b), which show the responses from 3 point targets located at $(x,z) = \{(0.40), (5,42), (-2,45)\}$ mm. The responses are simulated for a transducer of $M = 128$ elements using Field II [9], [10]. Fig. 3(a) shows the received sensor signals, $s_m(t)$, for $m = 0,1,\ldots,M-1$. In Fig. 3(b), the sensor signals are presteered at the point $\vec{r}_p = (0,40)$ mm. Due to the compensation for the delay line, the response from the focus point resembles a plane wave impinging directly onto the array. Thus, the presteered sensor signals will sum in phase, maximizing the DS beamformer output power at the focus point.

In the beamformer, the presteered sensor signals are weighted and subsequently summed. The amplitude of the

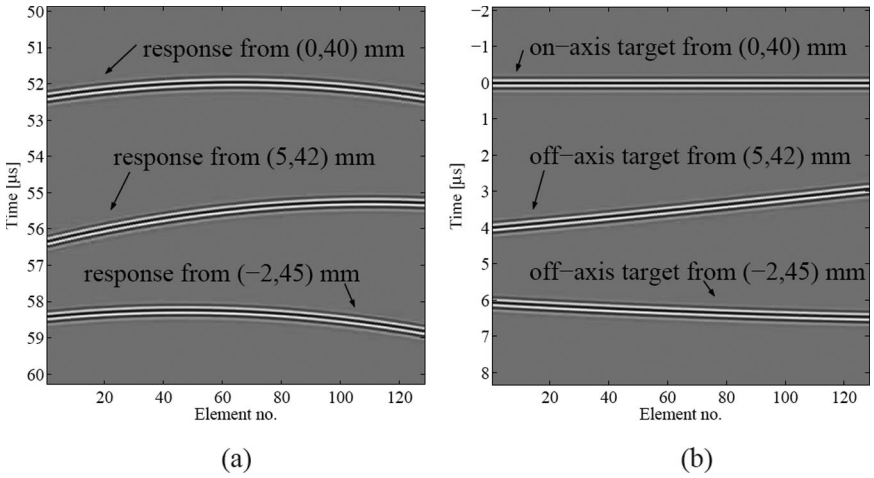

Fig. 3. (a) The received sensor signals, $s_m(t)$, for $m = 0,1,\ldots,M-1$. The figure shows the responses from 3 point targets located at $(x,z) = \{(0,40),(5,42),(-2,45)\}$ mm. (b) Sensor signals presteered at the focus point $\vec{r}_p = (0, 40)$ mm. After presteering, the response from the focus point resembles a plane wave impinging directly onto the array.

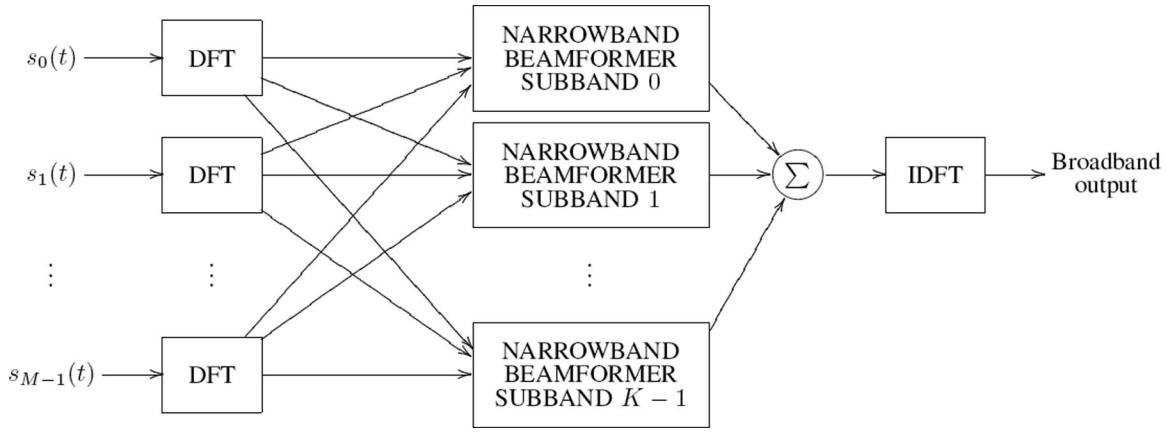

Fig. 4. Block diagram of a broadband beamformer. Each broadband sensor signal is divided into a set of narrowband signals using the discrete Fourier transform (DFT). Each frequency subband is processed independently by a narrowband beamformer. Subsequently, the processed subband responses are summed to provide the broadband beamformer output.

beamformer output at $t = 0$, provides the amplitude at the focus point $\vec{r}_p$ in the resulting beamformed image. Thus, the beamformer output is given by

$$b(\vec{r}_p) = \sum_{m=0}^{M-1} w_m y_m(0) = \sum_{m-0}^{M-1} w_m s_m(\tau_m(\vec{r}_p)), \qquad (3)$$

where w_m are the apodization weight on the mth sensor. Note that the apodization weights can be different for each focus point, but the dependence on $\vec{r}_p$ is here omitted. Whereas the conventional beamformer uses a set of predefined weights, the adaptive beamformer finds a set of optimized weights. The adaptive process for optimizing the apodization weights is described in Section II-C.

B. Subband Beamforming

The MV beamformer [1] was originally developed for narrow-band applications. As described in [11], the adaptive beamformer can be applied to broadband data by dividing the sensor signals into frequency subbands using the short-time, discrete Fourier transform (DFT). Each separate subband satisfies the narrowband condition of the adaptive beamformer and is processed independently, as illustrated in Fig. 4. First, the processed subband responses are summed, and then the inverse DFT is used to obtain the MV response from the focus point.

For each focus point, the DFT is applied on a segment of the presteered sensor signals. Due to the compensation for the delay line, the response from the focus point will be centered around $t = 0$, as seen in Fig. 3(b). The mth segmented, presteered sensor signal is thus given by

$$y_m(t) \text{ for } t \in [-t_d/2; t_d/2], \qquad (4)$$

where t_d is the time duration of the segment size. To sustain the axial resolution, t_d should not exceed the pulse length, which is given by the convolution of the excitation pulse and the 2-way impulse response of the transducer.

For the given focus point, the beamformer output for each frequency subband, ω, is given by

$$B(\omega,\vec{r}_p) = \sum_{m=0}^{M-1} w_m^*(\omega) Y_m(\omega), \tag{5}$$

where $Y_m(\omega)$ is the Fourier transform of the mth segmented sensor signal (4), and $\{\cdot\}^*$ denotes the complex conjugate. By defining the vectors

$$\mathbf{w}(\omega) = [w_0(\omega) \quad w_1(\omega) \quad \ldots \quad w_{M-1}(\omega)]^T \tag{6}$$

$$\mathbf{Y}(\omega) = [Y_0(\omega) \quad Y_1(\omega) \quad \ldots \quad Y_{M-1}(\omega)]^T, \tag{7}$$

the beamformer output (5) rewrites as

$$B(\omega,\vec{r}_p) = \mathbf{w}(\omega)^H \mathbf{Y}(\omega), \tag{8}$$

where the superscripts $\{\cdot\}^T$ and $\{\cdot\}^H$ denote the nonconjugate and the conjugate transpose, respectively. Note that the subband division provides the possibility of weighting both each subband and each point differently.

C. Minimum Variance Beamforming

The adaptive beamformer uses a set of apodization weights, which are dependent on the frequency content of the specific sensor signals. In the following, it is assumed that the sensor signals have been divided into frequency subbands as described in Section II-B

The MV beamformer continuously updates the weights, so that the power of the beamformer output is minimized, while the response from the focus point is passed without distortion. The power of the beamformer output is given by

$$\mathcal{P}(\vec{r}_p) = \mathcal{E}\left\{|B(\omega,\vec{r}_p)|^2\right\} \tag{9}$$

$$= \mathcal{E}\left\{|\mathbf{w}(\omega)^H \mathbf{Y}(\omega)|^2\right\} \tag{10}$$

$$= \mathcal{E}\left\{\mathbf{w}(\omega)^H \mathbf{Y}(\omega)\mathbf{Y}(\omega)^H \mathbf{w}(\omega)\right\} \tag{11}$$

$$= \mathbf{w}(\omega)^H \mathbf{R}(\omega)\mathbf{w}(\omega), \tag{12}$$

where $\mathcal{E}\{\cdot\}$ denotes the expectation value, and $\mathbf{R}(\omega)$ is the covariance matrix given by

$$\mathbf{R}(\omega) = \mathcal{E}\left\{\mathbf{Y}(\omega)\mathbf{Y}(\omega)^H\right\}. \tag{13}$$

Omitting the dependency on ω, the MV beamformer is expressed as [2]

$$\begin{aligned} &\min_{\mathbf{w}} \mathbf{w}^H \mathbf{R} \mathbf{w} \\ &\text{subject to } \mathbf{w}^H \mathbf{e} = 1, \end{aligned} \tag{14}$$

where $\mathbf{e}$ is the so-called steering vector, which characterizes the response from the focus point. The steering vector defines the signal that should be passed distortionless through the beamformer and is given by

$$e = \begin{bmatrix} \exp\{j\omega(\tau_0(\vec{r}_p) - \tau_0(\vec{r}_p))\} \\ \exp\{j\omega(\tau_1(\vec{r}_p) - \tau_1(\vec{r}_p))\} \\ \vdots \\ \exp\{j\omega(\tau_{M-1}(\vec{r}_p) - \tau_{M-1}(\vec{r}_p))\} \end{bmatrix} = \begin{bmatrix} 1 \\ 1 \\ \vdots \\ 1 \end{bmatrix}, \tag{15}$$

where $\tau_m(\vec{r}_p)$ is the delay line given in (1). Due to presteering, the sensor signals have already been compensated for the delay line, $\tau_m(\vec{r}_p)$. Thus, as illustrated in Fig. 3, the response from the focus point will resemble a plane wave incident directly onto the array. Thus, the steering vector is constant across the array and independent on the frequency, and it simply becomes a $M \times 1$-vector of ones.

The constrained optimization problem (14) can be solved analytically using Lagrangian multiplier theory [12]. Provided that $\mathbf{R}^{-1}$ exists, the MV optimized apodization weights are given by [1]

$$\mathbf{w} = \frac{\mathbf{R}^{-1}\mathbf{e}}{\mathbf{e}^H \mathbf{R}^{-1}\mathbf{e}}. \tag{16}$$

The subband MV beamformer output is found by applying these MV-optimized weights to the delayed sensor signals using (8). This yields an MV-optimized spectrum, and the amplitude corresponding to the focus point is found from the inverse Fourier transform of this spectrum and choosing the sample at $t = 0$.

D. Subarray Averaging

In real applications, the covariance matrix is unknown and must be replaced by the sample covariance matrix, which is estimated from the data. To estimate the sample covariance matrix, several realizations of data are required. In this paper, these realizations are obtained by dividing the data from a single acquisition into several subgroups. This follows the spatial smoothing approach suggested in [13].

As illustrated in Fig. 5, the spatially smoothed covariance matrix estimate is obtained by dividing the array into P overlapping subarrays of size $M_p \leq M/2$. For each subarray, a subcovariance matrix is estimated, and these are averaged across the array. The covariance matrix estimate can be expressed as

$$\mathbf{R} = \frac{1}{P}\sum_{p=0}^{P-1} \mathbf{G}_p \mathbf{G}_p^H, \tag{17}$$

where $\mathbf{G}_p$ denotes the pth subarray given by

TABLE I. PARAMETERS USED FOR THE FIELD II SIMULATIONS.

Transducer	
Transducer type	Linear array
Transducer element pitch	110 μm
Transducer element kerf	35 μm
Transducer element height	6 mm
Center frequency, f_0	7 MHz
Bandwidth	60% fractional
Speed of sound, C	1540 m/s
Wavelength, $\lambda = c/f_0$	220 μm
Excitation pulse	Two-cycle sinusoid at f_0
Synthetic Aperture Emission	
Transmit apodization	Hanning
Receive apodization	Boxcar/Hanning/MV
Number of transmitting elements	1
Number of receiving elements, M	128
Number of emissions	128
Plane Wave Emission	
Transmit apodization	Boxcar
Receive apodization	Boxcar/Hanning/MV
Number of transmitting elements	128
Number of receiving elements, M	128
Number of emissions	1
Linear Scan Emission	
Transmit apodization	Hanning
Transmit focus depth	45 mm
Receive apodization	Dynamic Hanning with $f/2.0$
Number of transmitting elements	128
Number of receiving elements, M	128
Number of emissions	185

$$\mathbf{G}_p = [Y_p(\omega) \quad Y_{p+1}(\omega) \quad \ldots \quad Y_{p+L-1}(\omega)]^T, \tag{18}$$

for $p = 0, 1, \ldots, P-1$. Note that this reduces the dimension of the covariance matrix, and thus the number of weights will be reduced correspondingly. The reduced weight vector $\tilde{\mathbf{w}}$ is applied to the data by averaging over the P subarrays, which is expressed as

$$B(\vec{r}_p) = \tilde{\mathbf{w}}^H \frac{1}{P} \sum_{p=0}^{P-1} \mathbf{G}_p, \tag{19}$$

Note that the reduced dimension also influences the resolution due to the inherent compromise between the width of the array and the achievable resolution [14].

III. APPLICATION TO ULTRASOUND DATA

The proposed MV beamformer is tested on simulated ultrasound data, obtained using Field II [9], [10]. For the simulations, a 7-MHz, 128-element linear array transducer with $\lambda/2$-spacing was used. The parameters for the simulations are given in Table I. In Section III-A, the method is applied to synthetic aperture data, and in Section III-B, data from a plane wave emission are used.

The MV beamformer is implemented in the frequency domain using the short time Fourier transform with a segment size corresponding to the length of the excitation pulse convolved with the 2-way impulse response of the transducer. A subarray size of $L = M/4 = 32$ was used. Before beamforming, additional white, zero-mean, Gaussian distributed noise with a signal-to-noise ratio (SNR) of 60 dB was added to each of the sensor signals.

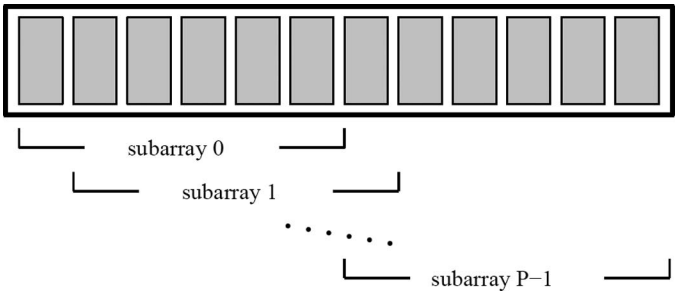

Fig. 5. Spatial smoothing. The array is divided into P overlapping subarrays, and the covariance matrix is averaged across the array.

The performance of MV is compared with DS using boxcar weights and Hanning weights. The performance is quantified by the full width at half maximum (FWHM) and the peak-side-lobe level (PSL), which is defined as the peak value of the first side-lobe.

A. Synthetic Aperture Emission

In this section, the proposed MV beamformer is tested using simulated synthetic aperture (SA) data. The concept of SA imaging is indicated in Fig. 6; a single element is used as the transmitting aperture and all $M = 128$ elements as the receiving aperture. The transmitting element is slid across the array, and for each single emission an image is created; these are traditionally referred to as low-resolution images [15]. Combining the single-emission images, obtained from the different spatial positions, provides an image with a higher resolution and contrast. A full SA sequence consisting of 128 emissions was simulated. Data for 13 point targets and for a circular cyst with a radius of 5 mm were simulated.

1) Point Targets: The beamformed responses of 13 point targets are shown in Fig. 8 with a dynamic range of 50 dB. Fig. 8(a) and (b) shows the DS beamformer responses using boxcar and Hanning apodization weights, respectively. The 3 responses in Fig. 8(a)–(c) are combined images from a full SA sequence. Thus, these have been averaged over 128 emissions. The MV response on the right, Fig. 8(d), is the response from a single emission, where a single element (element #64) was used as the transmitting aperture.

The lateral variation of the beamformed responses, Fig. 8, are shown in Fig. 7(a) and (b) at the depths $z = \{40, 45\}$ mm. As expected, it is seen that applying Hanning apodization weights to the DS beamformer reduces the side-lobe level at the expense of a lateral broadening of the main-lobe, compared with DS using boxcar weights.

The resolution and contrast improvements are quantified using the FWHM and PSL. These quantitative measures are calculated at a depth of 40 mm and are given in Table II. The measures are given for the single-element

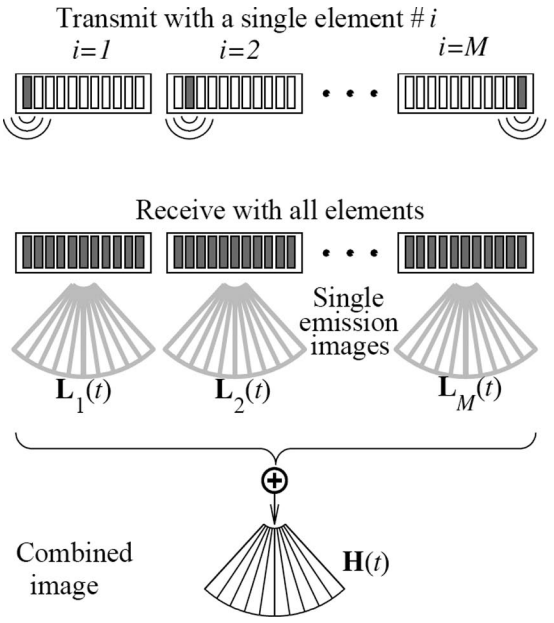

Fig. 6. Concept of synthetic aperture imaging. Several images are created from a single emission. These single emission images are averaged to obtain an image with a higher resolution and contrast. From [15].

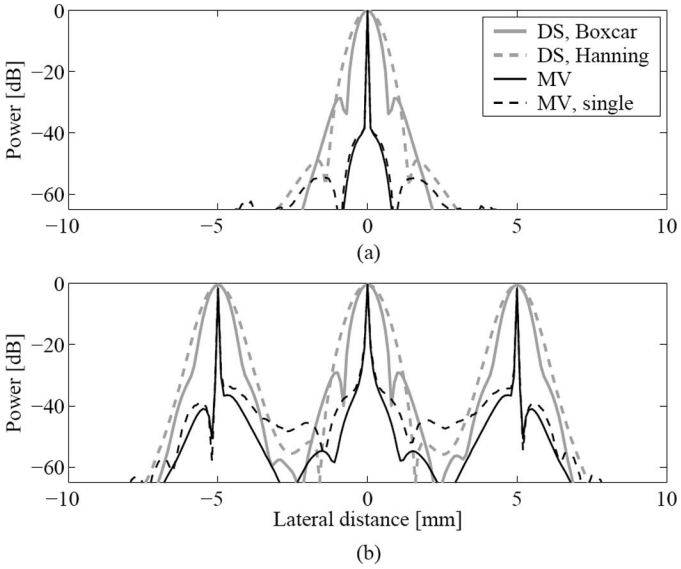

Fig. 7. Lateral variation at $z = 40$ mm (a), and 45 mm (b) of the beamformed responses shown in Fig. 8(a)–(d).

emission and for the full SA sequence. Only the lateral resolution has been considered, because the axial resolution does not change from that of the DS beamformer.

From Figs. 7 and 8 and Table II, it is seen that the MV beamformer provides a significant increase in the lateral resolution and a lowering of the side-lobes; it thus represents a significant improvement in terms of both resolution and contrast. The FWHM of MV from a single emission response comprise only {12.7%, 8.2%} of the FWHM from the full DS sequence using DS{boxcar, Hanning}.

As seen in Figs. 7(a)–(b), the MV response does not change significantly in the interval of [−40;0] dB. The FWHM is calculated at a level of −6 dB and will not change for MV, when averaging over all 128 emissions. This is shown in Fig. 10(a), where the FWHM for DS and MV are shown with respect to the number of emissions. Furthermore, the ratio of energy above and below −40 dB has been calculated relative to the number of emissions, shown in Fig. 10(b). A reduction of the relative energy within the main-lobe could mean that the width of the main-lobe decreases. It is seen that this ratio reduces with the number of emissions. However, the reduction for MV is not as large as for DS. Thus, the MV response does not improve significantly, when averaging over several emissions.

2) Circular Cyst: In this section, simulated data of a circular cyst in a speckle pattern are considered. The circular cyst has a radius of 5 mm and center at $(x,z) = (0,40)$ mm. The speckle pattern is simulated with 10 randomly placed scatterers within a resolution cell of $\lambda \times \lambda \times \lambda$ to ensure fully developed speckle, where λ is the wavelength given in Table I.

The beamformed responses for the full SA sequence are shown in Fig. 9(a)–(c). Thus, these responses are averaged over 128 emissions. In Fig. 9(d)–(f), the beamformed responses from a single emission are shown. These responses are from a emission using element #64 as the transmitting aperture. Furthermore, the lateral variation at a depth of $z = 40$ mm is seen in Fig. 11.

The single emission images, Figs. 9(d)–(f), emphasize the differences between the 3 beamforming approaches. It is seen that the high side-lobe level of the DS boxcar apodization results in a rather poor contrast. Furthermore, it is seen that the DS response using Hanning apodization does not result in a circular shape of the cyst. The shape is rather oval due to the lateral broadening from the Hanning apodization. However, the Hanning apodization does provide a suitable contrast level, because the side-lobes are lowered significantly. Note that in the combined images, Figs. 9(a)–(c), these effects have been averaged out. Thus, the side-lobe level has reduced for the DS boxcar response, and the circular shape of the cyst has been recovered for DS Hanning response.

The MV response from a single emission, Fig. 9(f), shows a circular shape of the cyst as well as a suitable contrast difference between the inner part of the cyst and the speckle pattern. From this investigation, it is seen that the MV beamformer provides a lowering of the side-lobe level without smoothing the responses laterally.

Only a slight difference can be observed between the single-emission MV response, Fig. 9(f), and the full SA sequence MV response, Fig. 9(c). In Fig. 11, this difference is easier to recognize. It is seen that the averaged responses have a reduced side-lobe level compared with the single emission responses. This is valid for all 3 approaches. However, it is seen that the single-emission MV response provides a side-lobe level, which is comparable to the averaged DS responses. Thus, the averaged MV

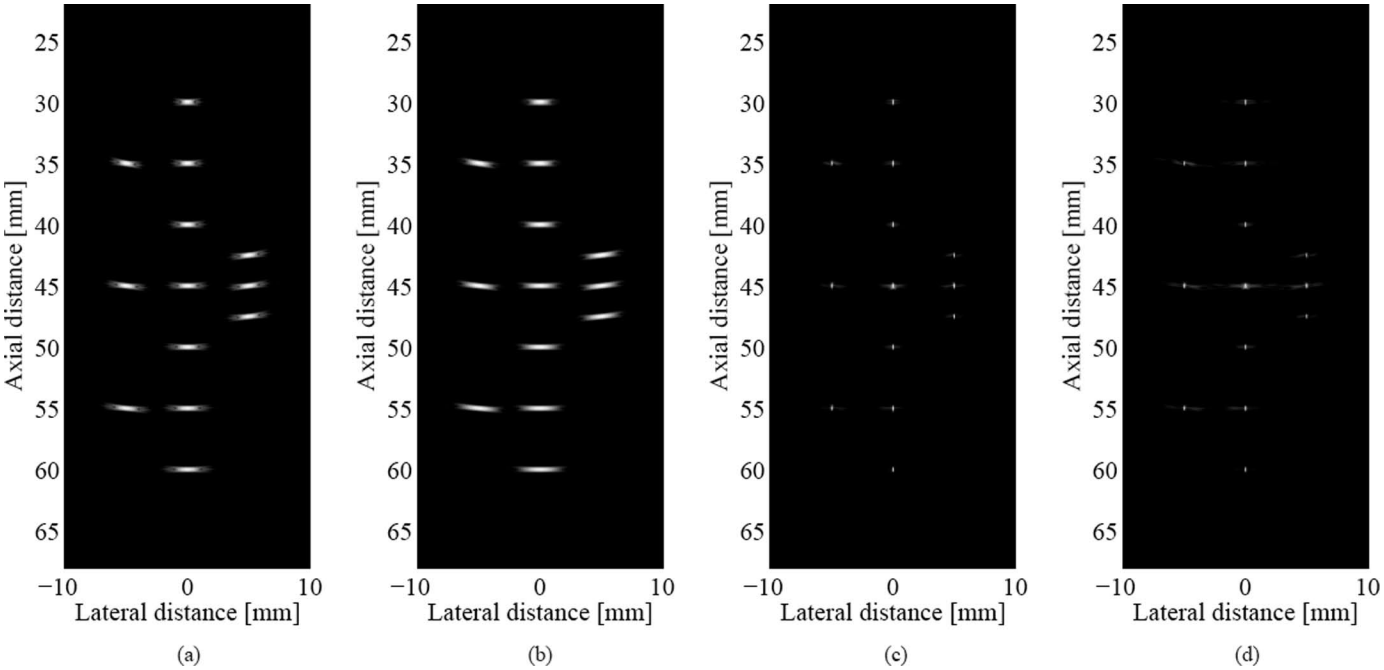

Fig. 8. Beamformed responses of the 13 point targets using simulated synthetic aperture data. (a) DS, Boxcar; (b) DS, Hanning; and (c) MV; the images are averaged over 128 emissions. (d) Response from a single element emission (element #64). All images are shown with a dynamic range of 50 dB.

TABLE II. FULL WIDTH AT HALF MAXIMUM (FWHM) AND PEAK-SIDE-LOBE LEVEL (PSL) FOR THE BEAMFORMED RESPONSES AT $z = 40$ MM.

	PSL	FWHM	
Single emission (element #64)			
DS, boxcar	−16 dB	0.79 mm	3.59λ
DS, Hanning	−36 dB	1.33 mm	6.05λ
MV	−49 dB	0.08 mm	0.36λ
Full sequence (averaged over 128 emissions)			
DS, boxcar	−32 dB	0.63 mm	2.86λ
DS, Hanning	−49 dB	0.97 mm	4.41λ
MV	−65 dB	0.08 mm	0.36λ

$\lambda = c/f_0 = 220$ μm.

response does provide a further reduction of the side-lobe level. This is substantiated by the estimated contrast levels for the 3 approaches, which are given in Table III. The contrast is computed as the ratio between the mean power within the cyst and outside the cyst.

B. Plane Wave Emission

A plane wave (PW) emission can be achieved by using all elements as both the transmitting and receiving aperture. In this way, the entire image region can be covered in a single emission. Note that when using PW, the propagation path from the transmitting element, $\vec{r}^{\,(\mathrm{xmt})}$, to the current image point, $\vec{r}_p = (x_p, z_p)$, in (1) simply becomes the axial distance, z_p, from the array to the image point

$$\left\| \vec{r}^{\,(\mathrm{xmt})} - \vec{r}_p \right\| = z_p. \tag{20}$$

The MV-beamformed response is compared with DS using boxcar and Hanning weights. The beamformed DS responses for the 13 point targets are seen in Fig. 12(b) and (c), and the MV response is seen in Fig. 12(d). The PW emission responses are compared with a conventional linear scan response. The linear scan image in Fig. 12(a) is obtained with a sliding aperture size of 128 elements and a fixed transmit focus at a depth of $z = 45$ mm. The response is beamformed using DS and dynamic Hanning apodization with $f/2$. The lateral variation of the beamformed responses, Fig. 12, are shown in Fig. 13 at depths of $z = \{40, 45\}$ mm. The FWHM and PSL are estimated at a depth of $z = 40$ mm and given in Table IV.

The PW data are obtained with boxcar apodization both in transmit and receive. This provides unwanted side-lobes below the point targets, as seen in Fig. 12(b) and (c). These could have been removed by using a transmit

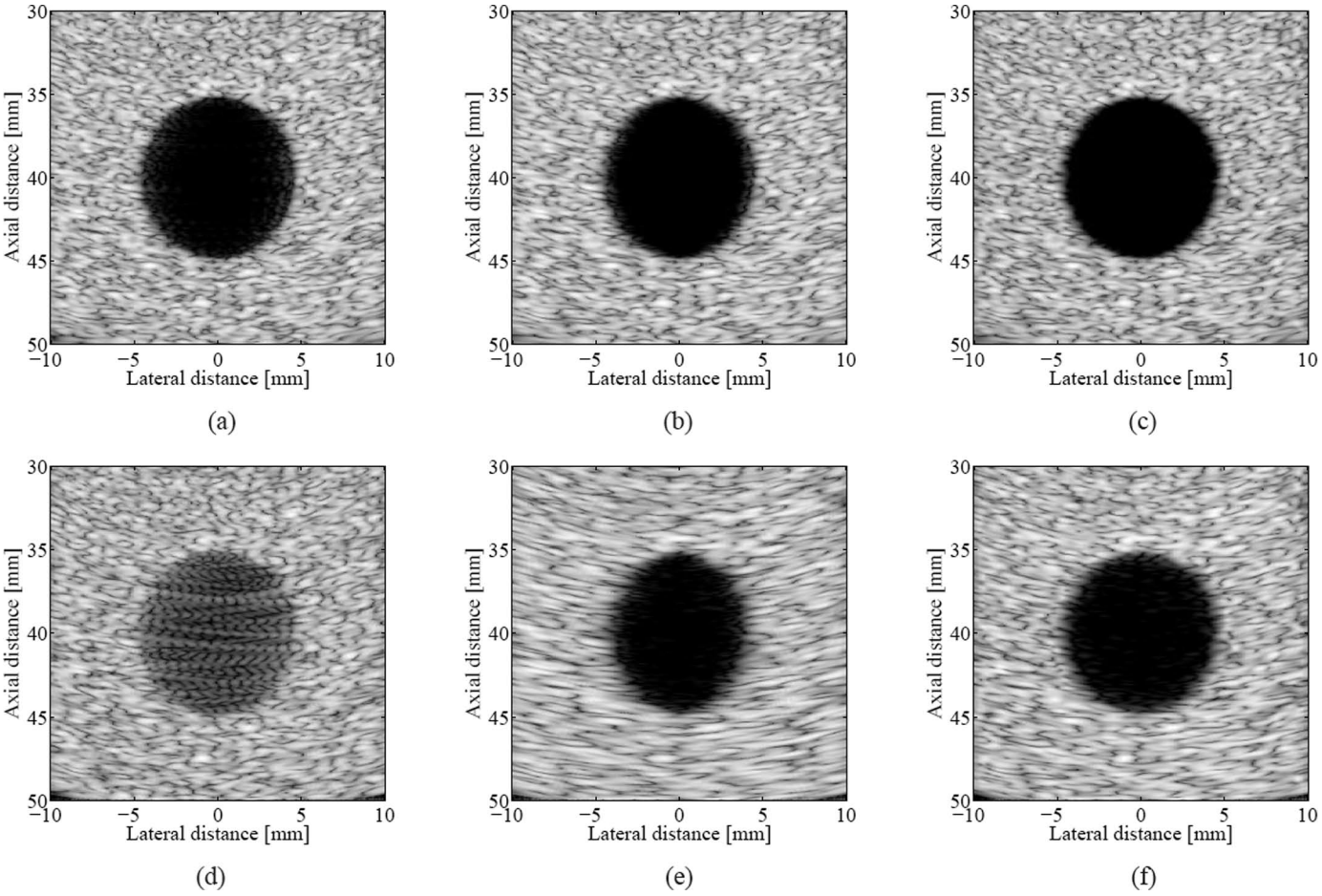

Fig. 9. Circular cyst with radius of 5 mm and center at $(x,z) = (0.40)$ mm. (a) DS, Boxcar; (b) DS, Hanning; and (c) MV; the images are the responses averaged over the full sequence of 128 emissions. (d) DS, Boxcar; (e) DS, Hanning; and (f) MV; the images are the responses to a single element emission (element #64). All images are shown with a dynamic range of 50 dB.

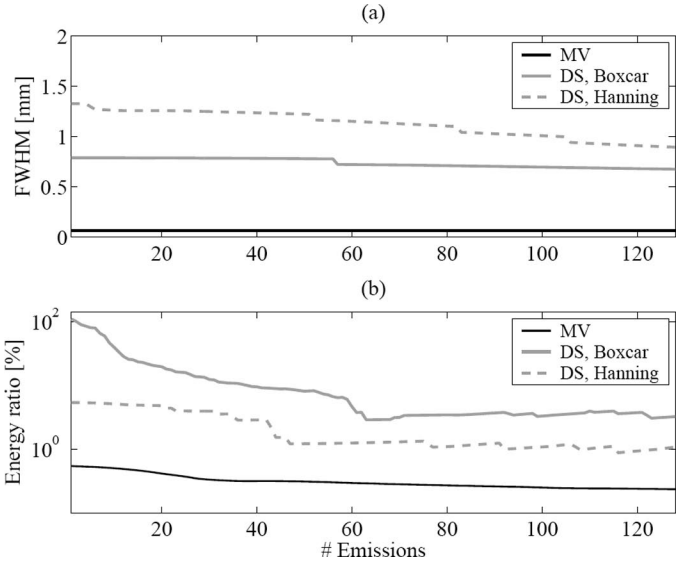

Fig. 10. Full Width at Half Maximum (FWHM) and the energy ratio above and below −40 dB of the beamformed responses with respect to the number of emissions.

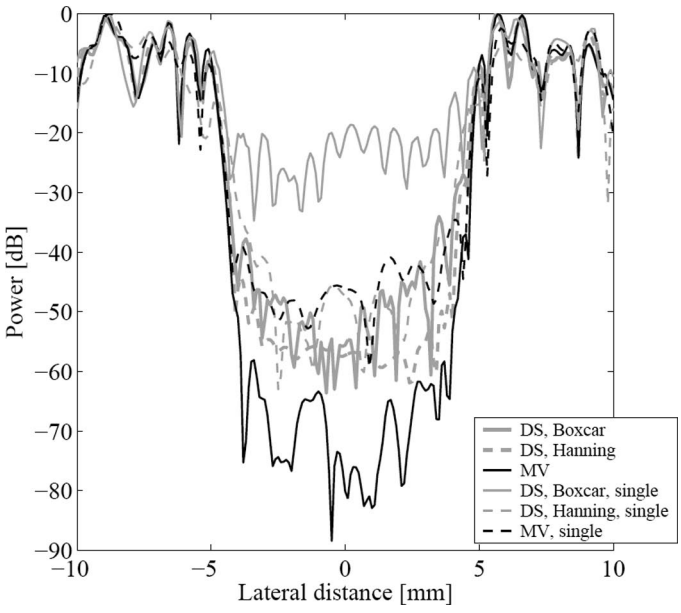

Fig. 11. Lateral variation at $z = 40$ mm of the beamformed responses in Fig. 9. The beamformed reponses in Fig. 9(a)–(c) are averaged over 128 emissions, and the responses in Fig. 9(d)–(f) are from a single emission.

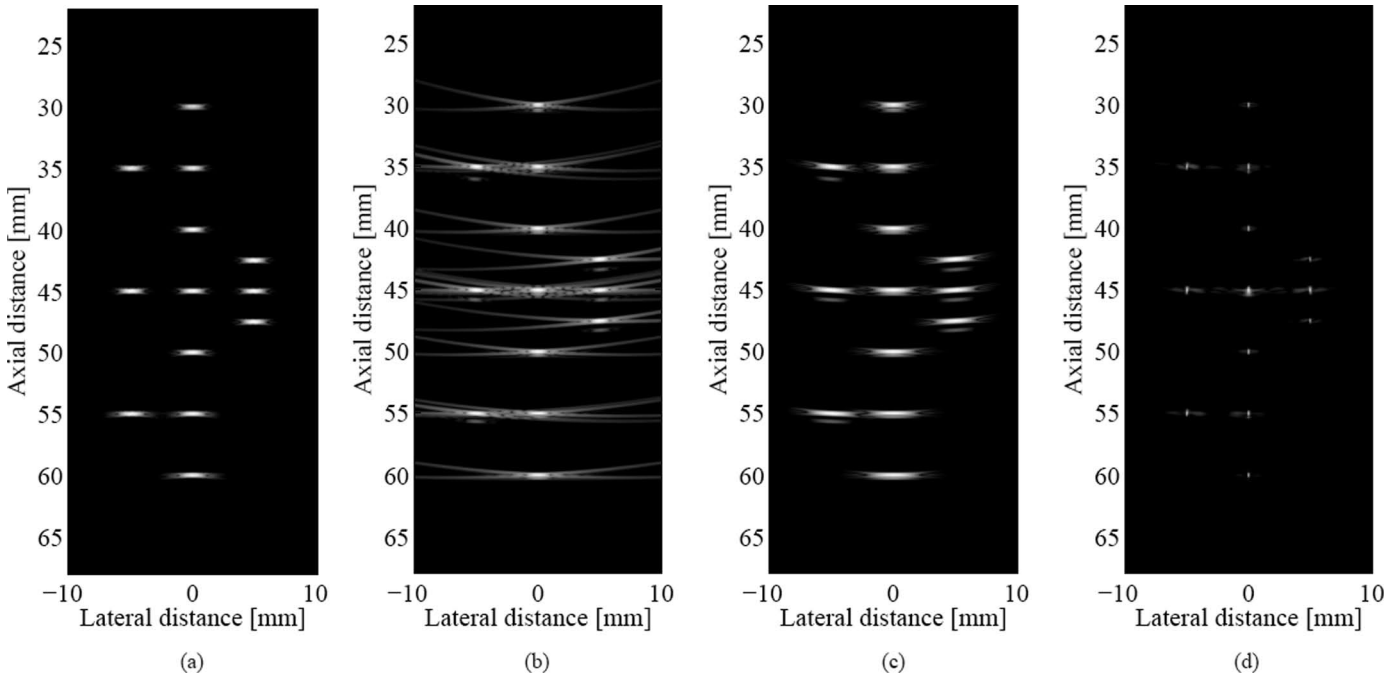

Fig. 12. Beamformed responses of the 13 point targets using simulated plane wave emission data. (a) Linear scan, DS beamformed using dynamic Hanning apodization with $f/2$; (b) DS, Boxcar; (c) DS, Hanning; and (d) MV plane wave emission images. All images are shown with a dynamic range of 50 dB.

TABLE III. CONTRAST LEVEL FOR THE CYST RESPONSES IN FIG. 9(A)–(F).

	Single emission	Full sequence
DS, Boxcar	−18 dB	−40 dB
DS, Hanning	−37 dB	−47 dB
MV	−40 dB	−60 dB

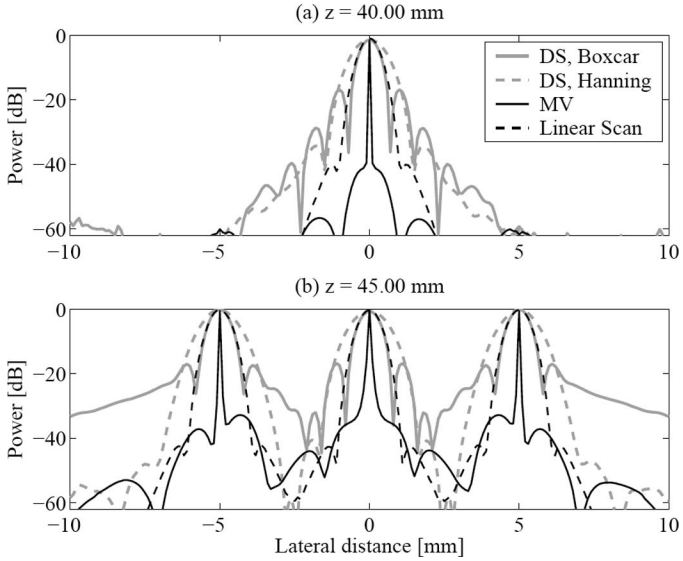

Fig. 13. Lateral variation at $z = 40$ mm (a) and 45 mm (b) of the beamformed responses shown in Fig. 8.

apodization, such as a Tukey window with 70% tapering as in [16]. However, this has not been done, to demonstrate the MV beamformer successes in eliminating these, as seen in Fig. 12(d).

Due to the focused emissions and the dynamic Hanning apodization, the linear scan sequence provides a more homogenous image than the unfocused PW transmissions. The resolution and contrast of the PW data are degraded, and the DS beamformed images are not acceptable for ultrasound imaging. The MV beamformer provides an increase of the resolution and contrast, as seen in Fig. 12(d) and Fig. 13. Even compared with the linear scan image, the MV beamformer provides a significant increase of the FWHM and PSL. From this investigation, it is seen that the increase of resolution and contrast, provided by the MV beamformer, yields the possibility of high-resolution and high-contrast PW imaging, where an image region can be covered in a single emission.

IV. THE EFFECT OF SOUND SPEED ERRORS

Adaptive beamformers are highly sensitive to steering vector errors. Robust approaches for adaptive beamforming are widely studied; see e.g., [11]. In medical ultrasound imaging, the primary cause of steering vector errors is incorrect sound speed estimates. Because this estimate varies with the characteristics of the different tissue types within the human body [17], the variation cannot be eliminated.

In the field of medical ultrasound imaging, robust methods for adaptive beamforming have been suggested by Wang *et al.* [7] and Synnevåg *et al.* [6]. However, no investigations on the performance reduction due to steering vector errors have yet been carried out.

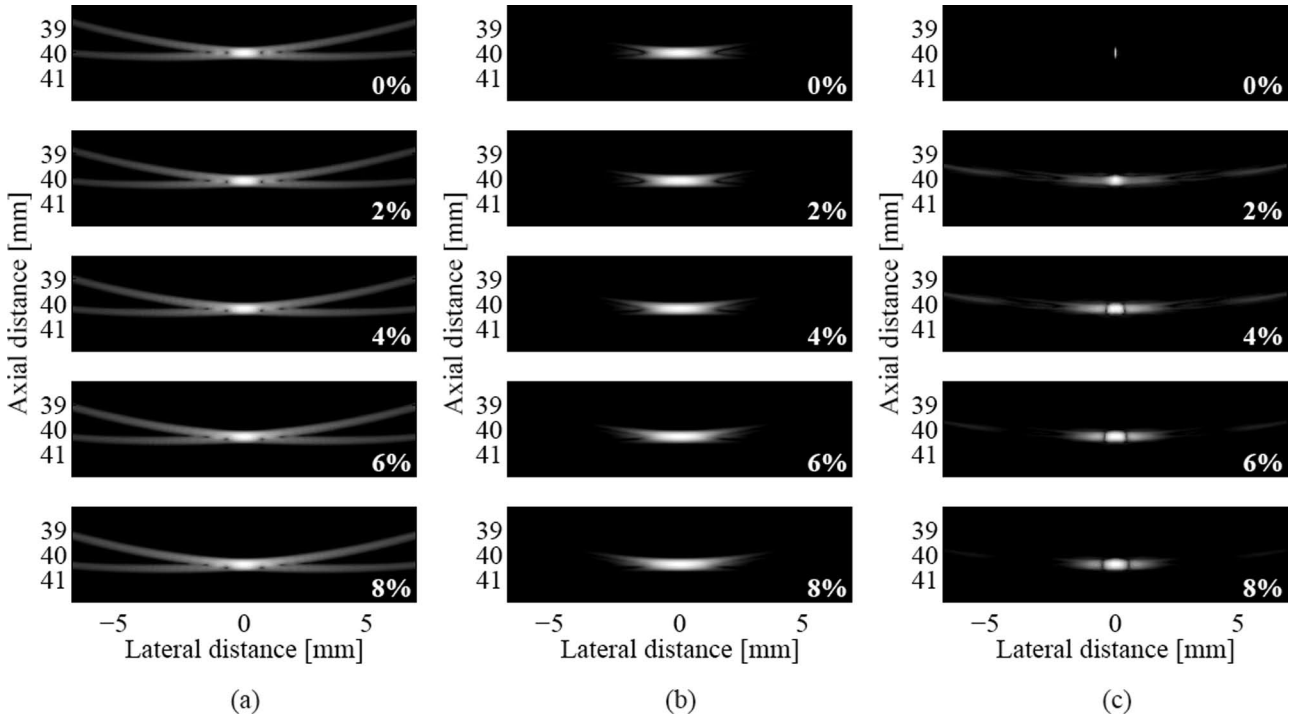

Fig. 14. Point spread functions (PSF) for the DS beamformer using boxcar (a) and Hanning (b) weights, and the MV beamformer (c) subjected to errors in the sound speed estimate. The percentage error is indicated on the lower right of each image. All images are shown with a dynamic range of 50 dB.

This section will investigate the effect of steering vector errors. The sound speed estimate is changed percentagewise from 0% to 20% of the true value. A selection of the resulting PSFs are seen in Fig. 14 with the lateral variation of the PSFs shown in Fig. 15(a)–(c). Furthermore, the FWHM with respect to the percentage error is shown in Fig. 15(d).

As described in the previous section, the top images of Fig. 14 and Fig. 15(a) show that the MV beamformer provides a significant increase in resolution and contrast compared with the DS beamformer. However, the sound speed estimate is required to be correct, an error of only a few percent degrades the potential performance significantly. As the error increases, it is seen that the MV beamformer is not as robust compared with the DS beamformer.

The FWHM in Table V is a measure of the main-lobe width and thus a measure of the resolution. It is seen that up to approximately 10%, the DS beamformer is rather robust, because the FWHM is rather constant with the percentage error of the sound speed estimate. It is noted that the DS does not outperform the MV beamformer within the investigated region of errors. In Fig. 15(d), it is seen that the FWHM for the MV beamformer does not become larger than that of the conventional beamformer.

The influence of sound speed errors cannot be ignored in medical ultrasound imaging. However, it is seen that the degradation of the performance of the MV beamformer does not lead to additional concerns beyond those that affect the DS beamformer. Thus, the adaptive beamformer can be implemented in the field of medical ultrasound imaging with the potential of increasing the resolution and contrast. This paper shows that incorrect speed of sound estimates will not lead to a performance degradation worse than that of the conventional DS beamformer.

TABLE IV. Full Width at Half Maximum (FWHM) and Peak-Side Lobe Level (PSL) for the Beamformed Responses at $z = 40$ mm.

	PSL	FWHM	
Linear Scan	−40.1 dB	0.82 mm	3.71λ
DS, Boxcar	−16.8 dB	0.71 mm	3.23λ
DS, Hanning	−34.4 dB	1.28 mm	5.81λ
MV	−57.0 dB	0.12 mm	0.53λ

$\lambda = c/f_0 = 220$ μm.

To obtain the potential increase in resolution and contrast, either robust methods should be applied or the sound speed should be estimated and compensated for [18].

V. Conclusions

An approach for near-field, adaptive beamforming of broadband data based on the minimum variance (MV) beamformer has been proposed. The approach is implemented in the frequency domain, and it provides a set of adapted, complex apodization weights for each frequency subband. The method is validated using Field II simulated synthetic aperture (SA) data and plane wave (PW) data. The performance of the MV beamformer is compared with the DS beamformer using boxcar and Hanning weights.

The adaptive subband beamformer provides a significant increase in resolution and contrast compared with

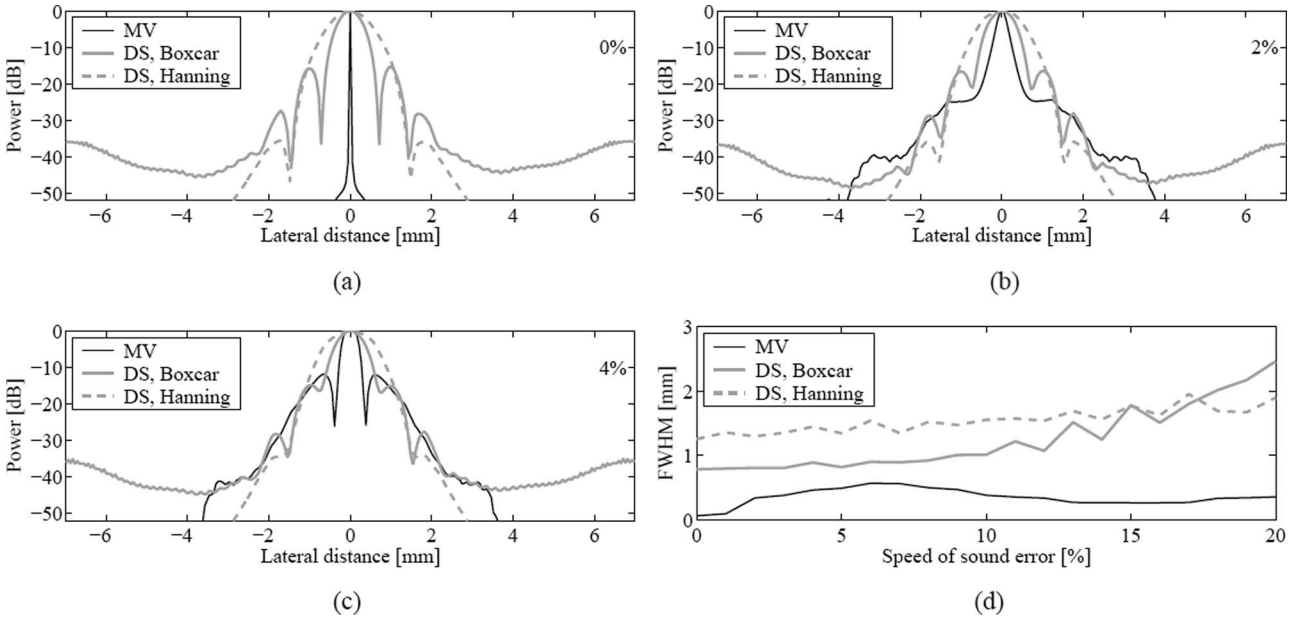

Figure 15. (a)–(c) Lateral variation of the PSF shown in Fig. 14(a)–(c), 0, 2, and 4%, respectively; (d) the FWHM with respect to the percentage error in the sound speed estimate.

TABLE V. Full Width at Half Maximum (FWHM) for the PSFs at the Depth of the Maximum Peak.

Error [%]		FWHM	
0%	DS, boxcar	0.78 mm	3.56λ
0%	DS, Hanning	1.25 mm	5.69λ
0%	MV	0.06 mm	0.29λ
2%	DS, boxcar	0.81 mm	3.67λ
2%	DS, Hanning	1.25 mm	5.89λ
2%	MV	0.34 mm	1.54λ
4%	DS, boxcar	0.89 mm	4.04λ
4%	DS, Hanning	1.44 mm	6.57λ
4%	MV	0.46 mm	2.10λ
6%	DS, boxcar	0.90 mm	4.08λ
6%	DS, Hanning	1.54 mm	7.00λ
6%	MV	0.57 mm	2.58λ
8%	DS, Boxcar	0.92 mm	4.18λ
8%	DS, Hanning	1.52 mm	6.91λ
8%	MV	0.50 mm	2.27λ
20%	DS, boxcar	2.46 mm	11.19λ
20%	DS, Hanning	1.90 mm	8.63λ
20%	MV	0.36 mm	1.61λ

$\lambda = c/f_0 = 220$ μm.

the conventional beamformer, even when using a single emission. It is seen that the resolution does not increase significantly when averaging several single emission images for MV. Thus, the MV beamformer introduces the possibility of imaging the entire region in a single emission using only a single emission.

Furthermore, the effect of steering vector errors originating from incorrect sound speed estimates on the performance of the MV beamformer has been investigated. The influence of sound speed errors cannot be ignored in medical ultrasound imaging. However, it is seen that the degradation of the performance of the MV beamformer does not lead to additional concerns beyond those that affect the DS beamformer. The achievable performance of MV is not outperformed by the conventional method.

References

[1] J. Capon, "High-resolution frequency-wavenumber spectrum analysis," *Proc. IEEE*, vol. 57, no. 8, pp. 1408–1418, Aug. 1969.

[2] J. A. Mann and W. F. Walker, "A constrained adaptive beamformer for medical ultrasound: Initial results," in *Proc. IEEE Ultrasonics Symp.*, Oct. 2002, vol. 2, pp. 1807–1810.

[3] O. L. Frost III, "An algorithm for linearly constrained adaptive array processing," *Proc. IEEE*, vol. 60, no. 8, pp. 926–935, 1972.

[4] M. Sasso and C. Cohen-Bacrie, "Medical ultrasound imaging using the fully adaptive beamformer," in *Proc. IEEE Int. Conf. Acoustics, Speech, and Signal Processing*, Mar. 2005, vol. 2, pp. 489–492.

[5] F. Viola and W. F. Walker, "Adaptive signal processing in medical ultrasound beamforming," in *Proc. IEEE Ultrasonics Symp.*, 2005, vol. 4, pp. 1980–1983.
[6] J.-F. Synnevåg, A. Austeng, and S. Holm, "Adaptive beamforming applied to medical ultrasound imaging," *IEEE Trans. Ultrason. Ferroelectr. Freq. Control*, vol. 54, no. 8, pp. 1606–1613, Aug. 2007.
[7] Z. Wang, J. Li, and R. Wu, "Time-delay- and time-reversal-based robust capon beamformers for ultrasound imaging," *IEEE Trans. Med. Imaging*, vol. 24, no. 10, pp. 1308–1322, Oct. 2005.
[8] I. K. Holfort, F. Gran, and J. A. Jensen, "Minimum variance beamforming for high frame-rate ultrasound imaging," in *Proc. IEEE Ultrasonics Symp.*, Oct. 2007, pp. 1541–1544.
[9] J. A. Jensen and N. B. Svendsen, "Calculation of pressure fields from arbitrarily shaped, apodized, and excited ultrasound transducers," *IEEE Trans. Ultrason. Ferroelectr. Freq. Control*, vol. 39, pp. 262–267, Mar. 1992.
[10] J. A. Jensen, "Field: A program for simulating ultrasound systems," *Med. Biol. Eng. Comp.*, 10th Nordic-Baltic Conference on Biomedical Imaging, vol. 4, suppl. 1, part 1, pp. 351–353, 1996b.
[11] J. Li and P. Stoica, *Robust Adaptive Beamforming*. New York: John Wiley & Sons, 2006.
[12] J. S. Arora, *Introduction to Optimum Design*. New York: McGraw-Hill, Inc., 1989.
[13] T.-J. Shan and T. Kailath, "Adaptive beamforming for coherent signals and interference," *IEEE Trans. Acoust. Speech. Sig. Pro.*, vol. 33, no. 3, pp. 527–536, Jun. 1985.
[14] D. H. Johnson and D. E. Dudgeon, *Array Signal Processing. Concepts and Techniques.* Englewood Cliffs, NJ: Prentice-Hall, 1993.
[15] S. I. Nikolov and J. A. Jensen, "In-vivo synthetic aperture flow imaging in medical ultrasound," *IEEE Trans. Ultrason. Ferroelectr. Freq. Control*, vol. 50, no. 7, pp. 848–856, 2003.
[16] J. Udesen, F. Gran, and J. A. Jensen, "Fast color flow mode imaging using plane wave excitation and temporal encoding," in *Proc. SPIE—Progress in Biomedical Optics and Imaging*, 2005, vol. 5750, pp. 427–436.
[17] S. A. Goss, R. L. Johnston, and F. Dunn, "Comprehensive compilation of empirical ultrasonic properties of mammalian tissues," *J. Acoust. Soc. Am.*, vol. 64, pp. 423–457, Aug. 1978.
[18] D. Robinson, J. Ophir, and C. Chen, "Pulse-echo ultrasound speed measurements: Progress and prospects," *Ultrasound Med. Biol.*, vol. 17, no. 6, pp. 633–646, 1991.

Iben Kraglund Holfort (S'08) was born in Viborg, Denmark, in 1980. She earned her M.Sc. degree in electrical engineering from the Technical University of Denmark in 2006. She is currently pursuing a Ph.D. degree in signal processing at the Technical University of Denmark.

Her research interests include array signal processing, adaptive beamforming, and blood flow estimation.

Fredrik Gran earned his M.Sc. in engineering physics from Lund University in 2002. In 2005, Dr. Gran received the Ph.D. degree from the Technical University of Denmark for work on ultrasound signal processing. From 2005 to 2008, he was employed as Assistant Professor at the Technical University of Denmark. In January 2008, Dr. Gran joined GN ReSound A/S as a research scientist in hearing aid signal processing.

His research interests include adaptive signal processing, adaptive beamforming, and acoustics.

Jørgen Arendt Jensen earned his Master of Science degree in electrical engineering in 1985 and the Ph.D. degree in 1989, both from the Technical University of Denmark. He received the Dr.Techn. degree from the university in 1996. He has published more than 160 journal and conference papers on signal processing and medical ultrasound and the book *Estimation of Blood Velocities Using Ultrasound*, Cambridge University Press in 1996. He is also developer of the Field II simulation program. He has been a visiting scientist at Duke University, Stanford University, and the University of Illinois at Urbana-Champaign. He is currently full professor of Biomedical Signal Processing at the Technical University of Denmark at the Department of Electrical Engineering and head of Center for Fast Ultrasound Imaging and the Group for Biomedical Engineering. He is also adjunct full professor at the Faculty of Health Sciences at the University of Copenhagen. He has given courses on blood velocity estimation at both Duke University and University of Illinois and teaches biomedical signal processing and medical imaging at the Technical University of Denmark. He has given several short courses on simulation, synthetic aperture imaging, and flow estimation at international scientific conferences. He has received several awards for his research.

He is also the co-organizer of B.Sc./M.Sc. education in biomedical engineering offered jointly by the Technical University of Denmark and the University of Copenhagen. His research is centered around simulation of ultrasound imaging, synthetic aperture imaging, vector blood flow estimation, and construction of ultrasound research systems.